

# Application of an acoustic analogy to PIV data from rectangular cavity flows

Christian Haigermoser

Received: 25 June 2008 / Revised: 4 February 2009 / Accepted: 4 March 2009 / Published online: 26 March 2009  
© Springer-Verlag 2009

**Abstract** The present paper describes a method to derive information about the acoustic emission of a flow using particle image velocimetry (PIV) data. The advantage of the method is that it allows studying sound sources, the related flow phenomena and their acoustic radiation into the far field, simultaneously. In a first step the time history of two-dimensional instantaneous pressure fields is derived from planar PIV data. In a successive step the Curle's acoustic analogy is applied to the pressure data to obtain the acoustic radiation of the flow. The test cases studied here are two rectangular cavity flows at very low Mach number with different aspect ratios  $L/H$ . The main sound source is located at the cavity trailing edge and it is due to the impingement of vortices shed in the shear layer. It is shown that the flow emits sound with a main directivity in the upstream direction for the smaller aspect ratio and the directivity is more uniform for the larger aspect ratio. In the latter case the acoustic pressure spectra has a broader character due to the impact of the downstream recirculation zone onto the shear layer instabilities, destroying their regular pattern and alternating the main sound source.

## 1 Introduction

Aerodynamically generated sound is an important issue in many engineering applications. In air transport, airframe noise has become more prominent as the engine noise has been reduced by 90% over the last 50 years (Neise 2004).

Today, the noise created by the high lift devices and the landing gear during approach is comparable to or louder than the noise emitted by the engines. High-speed train transport is also affected by aerodynamic noise, for example due to the presence of the gap between two train cars, which is a noise source. These are only a few examples out of many that explain the current research drive in aeroacoustics.

To investigate aeroacoustic sound sources, one has the choice to take an experimental, an analytical (Rona 2007) and/or a numerical approach. The latter can be done by solving the compressible Navier–Stokes equations, which include acoustics, by DNS. However, this approach suffers a few problems, one of them is that a high-accuracy computational scheme is needed to correctly resolve the acoustic part of the flow. Efforts are done using high-order methods (Tam 2004). Another problem is that the computational domain must include the source field and at least a part of the acoustic near field, leading to a large computational domain. The far-field propagation can then be obtained by either (1) extending the computational domain using an outer mesh to solve the linearized Euler equations (LEE) or (2) by using a Kirchhoff surface integral approach (Lyrintzis 1994).

The direct computation of sound using DNS is restricted to low Reynolds numbers and simple geometries. Therefore, it is more suitable for producing benchmark databases or developing theoretical models, rather than to predict the sound emission of an aeroacoustic problem. For a review on this subject see Colonius and Lele (2004).

Another approach to calculate sound is to use hybrid methods, where the sound is obtained in a successive step, after having calculated/measured the flow field. This approach was first introduced by Lighthill (1952) who considered the analogy between the propagation of sound

---

C. Haigermoser (✉)  
Politecnico di Torino, DIASP, Corso Duca degli Abruzzi 24,  
10129 Turin, Italy  
e-mail: christian.haigermoser@polito.it

in an unsteady unbounded flow to that in a uniform medium at rest, generated by a distribution of quadrupole acoustic sources. In this analogy, the flow governing equations, the Navier–Stokes equations, are replaced by an inhomogeneous wave equation, the Lighthill equation. The inhomogeneous part of the Lighthill equation models sound generation, attenuation, reflection, refraction, convection and scattering in the aerodynamic flow. Provided the inhomogeneous term, the Lighthill stress tensor, is known, the sound perceived by an observer  $P(x_i, t)$  in the far-field can be extracted by integrating the wave equation over the source field. This integration can be regarded as a post-processing of data obtained numerically or experimentally. The advantage of this approach is that the source term does not have to include the perturbations due to the linear acoustic propagation in the still flow and also that the sound sources do not have to be compact. Hence, this method allows to predict the aeroacoustic sound emission of a flow, by only knowing the fluid dynamics.

The drawback of the Lighthill acoustic analogy is that it does not account for the presence of solid boundaries in the flow. For this reason, the formulation was extended by Curle (1955) and then by Ffowcs Williams and Hawkins (1969) to take into account the generation and scattering mechanisms when solid bodies are present, see Sect. 3.

Another approach to investigate aeroacoustics is the experimental one, using mainly microphones and microphone arrays. Microphone arrays can directly measure the sound emission and locate the spatial position of its source. However, this method does not relate the sound emission to the aerodynamic unsteadiness responsible for its generation, unless the sound measurements are not synchronized with measurements of the flow field, using for example hot-wire anemometry or particle image velocimetry (PIV).

Recent improvements in PIV indicate that this technique is maturing towards providing higher spatial and time-resolved flow measurements. Furthermore, tomographic PIV (Elsinga et al. 2006a, b) may be able to describe with adequate resolution the source terms in the acoustic analogy so to extract the far-field sound using this approach.

The present study is a contribution towards developing and testing the extraction of far-field sound from time-resolved PIV flow-field measurements, using an acoustic analogy. As PIV only provides velocity measurements, part of the challenge is to extract synchronous estimates of the aerodynamic pressure distribution in the source region, which is required by the acoustic analogy. While the end goal is to predict sound from three-dimensional (3D) PIV data, this study uses less computer-intensive two-dimensional (2D) velocity data, which is the dataset available to the author.

The main contribution of using an acoustic analogy to extract far-field noise from PIV is that, whereas

synchronous PIV and microphone measurements can give the probability that a certain flow feature is linked to a far-field noise event, as determined for instance by cross-correlation, the acoustic analogy gives a deterministic route to linking the two. This is significant as it removes, by definition, the statistical ambiguity inherent to the cross-correlation approach, establishing a clear causality link between a flow feature and its noise. This opens the way to using experimental data to investigate sound sources and the related fluid dynamical phenomena and to explore changes in the flow that quiets it. This makes this and similar efforts towards extracting far-field noise from PIV data of significant scientific value.

In this paper, the PIV and acoustic analogy approach is applied to a cavity flow, where the noise generating mechanisms are well documented in the literature (Takeda and Shieh 2004). As the cavity test case includes surfaces, the Curle acoustic analogy was chosen, as explained in Sect. 3. The Curle acoustic analogy includes a volume integral over the Lighthill stress tensor and its time derivatives, plus a surface integral over the pressure and its time derivative on the body surface. Therefore, it is necessary to obtain the instantaneous pressure field from the PIV data, before applying the acoustic analogy, especially because it was shown that the volume integral contributes little to the overall sound emission from a low Mach number unsteady flow (e.g. Larsson et al. 2004). The instantaneous pressure fields are computed following essentially a method proposed by Liu and Katz (2006), see Sect. 2.

A brief overview of the state of the art of cavity flow physics is given below. Most of the current analytical models of cavity flow instability are for 2D rectangular cavities. A significant contribution to explain the unsteadiness of flows over rectangular cavities was given by Rossiter (1964). He identified an acoustic feedback mechanism for certain cavities and flow regimes. This feedback mechanism can be described as follows: A vortex is shed from the cavity leading edge and is convected downstream until it impinges onto the forward facing step, causing an acoustic pressure wave, which travels upstream and leads to instabilities in the shear layer and to the shedding of a new vortex. Rossiter developed an empirical formula to predict the resulting oscillation frequencies, which is based on previous studies on edge tones (e.g. Powell 1953, 1961):

$$f = \frac{U_e(m - \gamma)}{L(M + 1/k_c)} \quad (1)$$

where  $f$  is the frequency,  $U_e$  is the free-stream velocity,  $m$  is the integer mode number,  $\gamma$  is a factor accounting for the time lag between the passage of a vortex and the radiation of a pressure wave,  $L$  is the cavity length,  $M$  is the Mach number and  $1/k_c$  is the ratio between convection velocity of the vortices and the free-stream velocity. Rossiter and other

researchers found good agreement between the formula and experimental results for  $\gamma = 0.25$  and  $1/k_c = 1.75$ . He further identified a resonant mode, which occurs when the oscillations excite a proper acoustic mode, or organ pipe mode, of the cavity. The coupling between Rossiter and acoustic room modes is further detailed in Rona (2007).

The Rossiter model and its further developments (see the review by Rockwell and Naudasher 1978), attempt to derive acoustic feed-back mechanisms that predict the dominant frequencies. These models are adequately successful in the case of shear-layer driven cavity flows. This flow regime is present at low cavity length to depth ratio ( $L/H$ ) and at reasonably high Mach and high Reynolds numbers, where the flow above the cavity is relatively undisturbed and the main unsteady flow feature is the convection of vortices in the shear layer, as detailed by Tam and Block (1978). Instead, at low Mach numbers, the flow oscillations are driven by convective waves rather than by shed vortices as discussed by Sarohia (1977) and by Chatellier et al. (2004).

Another flow mode was found by Gharib and Roshko (1987) at high  $L/H$  and when the length and/or depth of the cavity becomes large with respect to the upstream boundary layer thickness. In this so-called wake mode the flow behaves more like the wake of a bluff body, than a free shear layer. The flow becomes more violent and unsteady. A vortex that fills about the whole cavity is formed at the leading edge of the cavity and when it is large enough it is released above the trailing edge. In this regime the flow above the cavity is affected by the flow inside the cavity and free-stream fluid is periodically directed into and out of the cavity (e.g. Larsson et al. (2004)). This flow regime is connected to a large increase in drag.

Many researchers have tried to determine parameters to indicate the occurrence of the different cavity flow modes. The main parameter considered to predict the existence of peaks in the pressure spectra is the ratio  $L/\theta$  (Grace et al. 2004), where  $\theta$  is the upstream boundary layer momentum thickness. However, experimental results are often in contrast, which may be due to the abundance of other geometrical and physical quantities involved, such as Reynolds number, Mach number, upstream boundary layer structure and 3D effects. Several researchers have studied the noise radiation from rectangular cavities. Ahuja and Mendoza (1995) measured the noise radiation from rectangular cavities and its dependence on the width to depth and length to depth ratios. They found that shallow cavities have a more uniform directivity of noise radiation than deep cavities, which have a main directivity of  $50^\circ$ – $60^\circ$  azimuth in streamwise direction. Colonius et al. (2001) investigated rectangular cavities of different aspect ratio at Mach numbers ranging from 0.2 to 0.8 and found that the cavities radiate noise directionally at a preferential azimuthal angle of about  $135^\circ$ . Similar results were obtained by Rowley et al.

(2001), Gloerfelt et al. (2003) also found that the peak noise directivity is around  $120^\circ$  for a  $L/H = 2$  cavity at a high subsonic Mach number. Larsson et al. (2004) investigated numerically the noise radiation of a cavity with  $L/H = 4$  at  $M = 0.15$  applying the Curle acoustic analogy to the 2D numerical data. The flow was found to be in the wake mode regime, which is often the case in 2D numerical simulations (Colonius et al. 2001; Shieh and Morris 1999; Gloerfelt et al. 2003). He predicted a minimum sound pressure level (SPL) in the near field above the cavity trailing edge and a strong noise radiation in the upstream direction. He also predicted a secondary directivity in downstream direction.

Takeda and Shieh (2004) provide a review on the use of computational aeroacoustics in connection with cavity flows. For a general review of cavity flows, see Rockwell and Naudasher (1978), Komerath et al. (1987), and Rowley and Williams (2006).

## 2 Obtaining the pressure from planar PIV data

This section describes the numerical procedure to derive the static pressure field from 2D velocity fields obtained by PIV, following a similar approach as that of Liu and Katz (2006). In contrast to Liu and Katz (2006), in the present case no four exposure PIV systems and no vector alignment is needed, as time-resolved PIV data of the flow is available. It is also pointed out that with the present PIV setup and especially the type of seeding used, no velocities induced due to acoustic pressure fluctuations can be resolved, meaning that the here obtained planar velocity fields contain only the fluid dynamics. In the following, the method introduced by Liu and Katz is summarized shortly. Two approaches to obtain the static pressure distribution are available, based respectively on the Poisson equation and on the Navier–Stokes momentum equations. The Poisson equation approach requires 3D velocity data, which were not available to the authors. A 2D projection of the Poisson equation involves computing the velocity vector second-order derivative and this can introduce large numerical errors. The other approach involves the incompressible Navier–Stokes momentum equations, where the pressure gradient can be expressed as

$$\nabla p = -\rho \left( \frac{D\mathbf{U}}{Dt} - \nu \nabla^2 \mathbf{U} \right) \quad (2)$$

and

$$\frac{D\mathbf{U}}{Dt} = \frac{d\mathbf{U}}{dt} + \mathbf{U}\nabla\mathbf{U} \quad (3)$$

is the material derivative of the velocity vector  $\mathbf{U}$ . An evaluation of at least the in-plane components of the viscous term in Eq. 2 shows that its contribution is negligible compared to the material derivative contribution (see also Liu and Katz 2006).

In Eq. 2, the material derivative term can be estimated in either the Lagrangian or the Eulerian frame of reference, respectively by evaluating the left hand side or the right hand side of Eq. 3. The Eulerian form involves 3D velocity vectors and their gradients, which are not available in planar PIV data. By maintaining the material derivative in the Lagrangian form, this problem can be overcome as only the material in-plane accelerations are necessary in order to obtain the in plane pressure gradients. The pressure gradient can then be integrated in space to obtain the static pressure distribution in the measurement plane. Note that pressure is a scalar and continuously differentiable, therefore the integration of its gradient must be independent of the integration path. Therefore, the out-of-plane pressure gradient is not required.

The material acceleration is computed following the procedure in Liu and Katz (2006). The choice of  $\delta t$ , which is the time between the two velocity fields used for the computation of the acceleration, is important for the accuracy of the acceleration measurement. A large  $\delta t$  would result in a higher risk of a loss of particles from the first instant to the next due to an out-of-plane motion, whereas a small  $\delta t$  would result in a higher uncertainty of the acceleration measurement (see Jensen and Petersen 2004). The maximum instantaneous out-of-plane velocity of the present cavity flow is assumed not to be larger than 60% of the freestream velocity, here  $U_e = 0.4$  m/s. The light sheet thickness is about 1 mm and the chosen  $\delta t$  is 0.004 s, corresponding to a separation of four frames in the velocity field time history. The maximum out-of-plane displacement can be estimated to be slightly lower than 1 mm at the above measurement and flow conditions, which is a conservative estimate. It was seen that the noise in the acceleration measurement was significantly reduced using this large  $\delta t$ . The time separation of the velocity fields to calculate the Lagrangian acceleration should be evaluated for each specific experiment in order to minimize the evaluation error. The material acceleration fields are successively integrated in space using a *virtual boundary integration method* (Liu and Katz 2006). The reason to use this kind of integration is that a direct solution, which can be obtained by solving a least square problem is not possible. The known material acceleration and the pressure are related by discrete differential equations, which form an over-determined matrix equation. However, the solution of such a matrix equation by matrix iteration (Southwell 1980), direct matrix inversion (Herrmann 1980) or singular value decomposition (Press et al. 2002) needs experience and is also computationally expensive (Liu and Katz 2006). To overcome this problem, the *virtual boundary integration method* (Liu and Katz 2006) is used, where a circular buffer zone is built around the data field, as shown in Fig. 1.

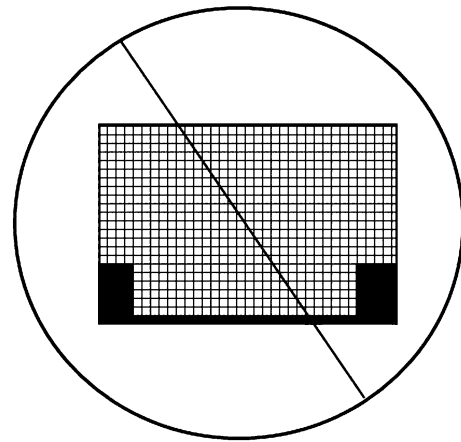


**Fig. 1** Buffer zone for the virtual boundary integration method

Further, all points along the boundary are connected with each other by lines. A shortest path integration is then performed along the lines which intersect the data field, starting from the first point of the boundary of the data field. Obviously, a first predictor of the pressure field at least along the data field boundaries must be known. Therefore, an initial integration is done, starting from a point in the free-stream, where the pressure is set to a constant, here  $p = 0$ . From this point the integration goes in four directions, up, down, left and right, obtaining two lines of pressure values in the field. From all new data points along these lines the integration continues respectively in all directions. If a point is crossed by the integration two times, a mean pressure value is calculated. After this first quick integration the above algorithm starts and every time a new pressure value is obtained at a location, the weighted mean of the new value and the old value is built. The pressure fields in the present work were obtained building a circular buffer zone with a radius equal to the length of the data field in  $x$  direction and its center in the center of the data field. A total of 180 points along the boundary of the buffer zone were connected to each other and the above described integration algorithm was applied. In the whole procedure the area inside the cavity walls was masked out.

The resulting pressure time series was then filtered using a second-order polynomial space–time filter with a spatial kernel size of  $5 \times 5$  grid points and a time kernel of seven snapshots. To account for the presence of the cavity walls, across which the static pressure can be discontinuous, the filter kernel did not include points inside the walls. The method was tested using synthetic velocity fields from a monopole acoustic source, where the velocity components can be expressed as

$$U(x, y) = u_r \frac{x}{R} \quad (4)$$

and

$$V(x, y) = u_r \frac{y}{R} \tag{5}$$

with

$$u_r = \frac{A}{(R \times \rho \times \omega)} \times \left( \frac{1}{R} \cos(\omega \times (t - R/c_0)) + \frac{w}{c_0} \sin(\omega \times (t - R/c_0)) \right) \tag{6}$$

where  $A$  is a constant,  $\rho$  is the density,  $\omega$  is a frequency,  $R$  is the distance from the center of the monopole and  $c_0$  is the speed of sound. The acoustic pressure fluctuation is obtained by

$$p(x, y) = \frac{A}{R} \cos(w \times (t - R/c_0)) \tag{7}$$

The spatial resolution was 18 points per wavelength and the temporal resolution was 30 samples per period, chosen to be similar to the space time resolution of the large scale structures inside the shear layer. In Fig. 2 the difference between the pressure fluctuation  $p$  predicted by the virtual boundary integration method and the analytical solution  $p_a$  is shown, normalized by the maximum pressure amplitude in the field  $p_{ref}$ . Figure 2 shows that the maximum difference is below 2%. Introducing white noise with a maximum amplitude of percentage of the maximum velocity in the data field, the error of the resulting pressure remains nearly as low as before, as shown in Fig. 2b. Obviously, the error increases approaching the center of the monopole, where the velocity gradients are stronger.

Starting from a time-series of PIV images as obtained by a time-resolved PIV measurement, this section has shown how to obtain a time series of velocity fields from which a time series of material acceleration fields is derived. Finally, a time series of instantaneous pressure fields is obtained by the virtual boundary integration method. The application to a single monopole radiation test case has shown good agreement between the pressure fluctuation obtained by this method and the reference analytical solution.

### 3 Estimating the sound emission using planar PIV data

In 1952, Lighthill (1952) introduced a method to obtain the acoustic emission from a flow using an inhomogeneous scalar wave equation. The equation consists of a source term on the right hand side and of a wave operator on the left hand side. It is obtained by differentiating the continuity equation with respect to time, subtracting the divergence of the momentum equations giving and adding the term  $-a_\infty \partial^2 \rho / \partial x_i^2$  to obtain:

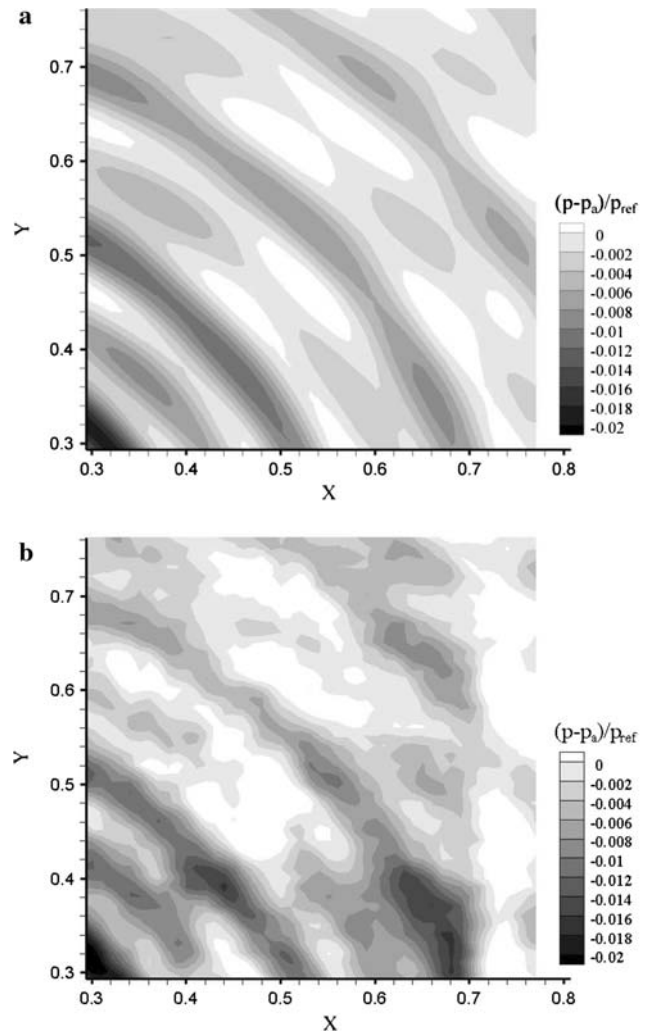


**Fig. 2** Error evaluation of calculation of instantaneous pressure. **a** Error in acoustic pressure fluctuation without added noise. **b** Error in acoustic pressure fluctuation with added noise of 5% of the maximum velocity in the field

$$\frac{\partial^2 \rho}{\partial t^2} - a_\infty^2 \frac{\partial^2 \rho}{\partial x_i^2} = \frac{\partial^2 T_{ij}}{\partial x_i \partial x_j} \tag{8}$$

where  $T_{ij} = \rho u_i u_j - \tau_{ij} + (p - a_\infty \rho) \delta_{ij}$  is the Lighthill stress tensor. The Lighthill analogy does not include the effect of solid boundaries in the flow, thus it considers only aerodynamically generated sound without solid body interaction. This limitation was overcome by Curle (1955), who formulated an analogy for non-moving solid bodies:

$$\rho(x, t) - \rho_\infty = \frac{1}{4\pi a_\infty^2} \frac{\partial^2}{\partial x_i \partial x_j} \int_V \frac{T_{ij}}{r} dV(y) - \frac{1}{4\pi a_\infty^2} \frac{\partial}{\partial x_i} \int_S \frac{n_j}{r} (p \delta_{ij} - \tau_{ij}) dS(y) \tag{9}$$

where  $\delta_{ij}$  is the Kronecker delta function. Equation 3 shows two terms on the right hand side, a volume and a surface

integral. Sarkar and Hussaini (1993) suggests that temporal derivatives of the source term are preferable to spatial derivatives. Therefore, Eq. 3 is modified giving the final result of this transformation (Larsson et al. 2004):

$$\begin{aligned}
 p(x, t) - p_\infty = & \frac{1}{4\pi} \int_V \left[ \frac{l_i l_j}{a_\infty^2 r} \ddot{T}_{ij} + \frac{3l_i l_j - \delta_{ij}}{a_\infty r^2} \dot{T}_{ij} \right. \\
 & \left. + \frac{3l_i l_j - \delta_{ij}}{r^3} T_{ij} \right] dV(y) \\
 & + \frac{1}{4\pi} \int_S l_i n_j \left[ \frac{\dot{p}\delta_{ij} - \dot{\tau}_{ij}}{a_\infty r} + \frac{p\delta_{ij} - \tau_{ij}}{r^2} \right] dS(y)
 \end{aligned}
 \tag{10}$$

where  $l$  is a unit vector pointing from the source to the observer and  $n$  is a unit vector normal to the bodies surface.

The main source of sound generation in a low Mach number cavity flow is the interaction of the flow with the cavity walls. Specifically, the vortices shed from the cavity leading edge create pressure fluctuation when they impinge onto the cavity forward facing step. These surface pressure fluctuations make the surface integral contribution to far-field noise dominant with respect to that of the volume integral. Larsson et al. (2004) investigated, in his numerical study, this assertion by evaluating all the terms in the Curle acoustic analogy applied to a cavity flow and concluded that the volume integral contribution is indeed negligible. This is in agreement with Curle’s dimensional analysis (Curle 1955) that the dipole sources along the wall become increasingly important at decreasing Mach numbers over the quadrupole sources. Further, in the present case the viscous stress tensor was evaluated and it was shown that it is also negligible. Equation 3 is derived for a 3D space. As the pressure fields obtained from the present PIV data are only available in a 2D plane, Eq. 3 is integrated in the out-of-plane direction from  $-w$  to  $w$ , where  $w$  is half the cavity spanwise extension, yielding

$$p(x, t) - p_0 = \frac{1}{4\pi} \int_L l_i n_j \left[ 2\arctan(w/r) \frac{\dot{p}\delta_{ij}}{a_\infty} + 2w \frac{p\delta_{ij}}{r^2} \right] dL(y).
 \tag{11}$$

The surface integral becomes a line integral along the cavity walls. In this way it is assumed that the flow is 2D and uniform in the spanwise direction. The integral in Eq. 11 has to be evaluated at the retarded time  $\tau$ .

Finally, for the computation of the acoustic pressure received by different observers only source points which lie in a direct line of sight from the observer to the source are considered. Other sources are not considered. The problem studied in this paper consists of cavity flows at a low free-stream Mach number. Under these conditions, ignoring the small Doppler effect on the acoustic radiation

due to the free stream velocity, the Curle acoustic analogy can be used.

The planar PIV time-resolved experiments were carried out in a water tunnel at the Politecnico di Torino with a test section of  $350 \times 350 \text{ mm}^2$ . Figure 3 shows the cavity model in the tunnel test section. The cavity depth  $H$  was 10 mm, the chosen aspect ratios were  $L/H = 3$  and  $L/H = 4$  and the freestream velocities were  $U_e = 0.26 \text{ m/s}$  and  $U_e = 0.36 \text{ m/s}$ , respectively. The incoming boundary layer was laminar with the characteristics as summarized in Table 1. The ratio  $L/\theta$  was 49 and 59, which is below the  $L/\theta > 80$  threshold for the onset of self-sustained cavity oscillations, as determined by Gharib and Roshko (1987), but oscillations developed in the present cavity flow despite this low  $L/\theta$  ratios.

Particle image velocimetry measurements were taken in streamwise planes normal to the cavity floor at the cavity mid-span. The field of view covered the whole cavity and the complete boundary layer up to the region of undisturbed flow outside the boundary layer.

The PIV setup consisted of a continuous Spectra-Physics Argon-Ion laser with a maximum emitted beam power of 6 W, illuminating the measurement plane with a laser light sheet 1 mm thick. The flow was seeded with hollow glass spheres with a nominal diameter of 10  $\mu\text{m}$ .

The particle image size was approximately 3 pixels at  $f_\# = 2.8$ . The PIV images were acquired using a Dantec MK III CMOS camera with a resolution of  $1,280 \times 1,024$  pixels and a maximum recording rate at full resolution of 1,000 fps, which was the acquisition rate used in the

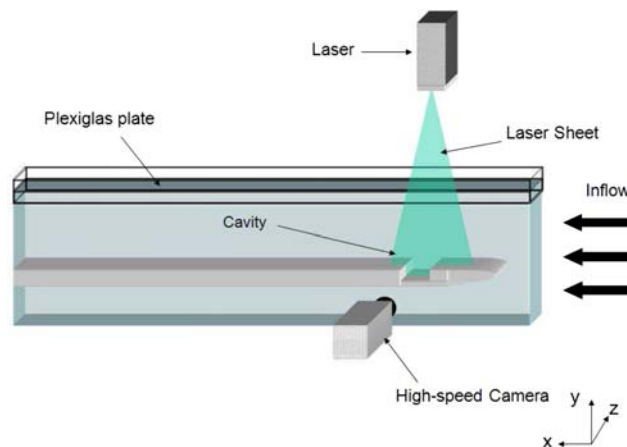


Fig. 3 Experimental setup

Table 1 Inflow conditions

$L/H$	$U_e$ (m/s)	$\delta$ (mm)	$\theta$ (mm)	$Re_L$	$L/\theta$	$\delta/H$
3	0.26	2	0.6	7,800	49	0.2
4	0.36	1.5	0.7	10,800	59	0.15

experiment. The camera has an internal memory of 4 GB, which limited the acquisition time at 1,000 fps at full resolution and at single exposure to 3.2 s giving 3,200 images.

Two successive images were cross-correlated to obtain the velocity field using a multigrid algorithm provided by the DAVIS 7.2 software from LaVision with an initial interrogation window size of  $128 \times 128$  pixels and a final interrogation window size of  $32 \times 32$  pixels with a 50% overlap, applying sub-pixel refinement and window deformation. Hence, one vector corresponds to the velocity in a spatial area of  $0.8 \times 0.8 \text{ mm}^2$  in case of  $L/H = 3$  and  $1 \times 1 \text{ mm}^2$  in case of  $L/H = 4$ .

The error in measuring the flow velocity with PIV depends on the particle image size, the particle image density and the velocity gradient. Based on the present images, the error in measuring the particle displacement between two images is less than 0.1 pixels. With a displacement from one image to the successive one of more than 10 pixels in the outer flow and about half of it in the shear layer, the error in measuring the velocity is less than 2%.

## 4 Results

### 4.1 Mean and instantaneous quantities

In this section the cavity flow physics is summarized. A more exhaustive description is given in Haigermoser et al. (2008). In Fig. 4 the streamlines of the mean velocity fields are shown, indicating the presence of a large recirculation zone in the downstream part of the cavities and a smaller one in the upstream part. In Fig. 5 the lateral component of the 2D Reynolds stress is shown normalized by the free-stream velocity  $U_e$ . The Reynolds stress grows downstream of the cavities leading edge along the shear layer. The maximum Reynolds shear stress occurs at about is  $-0.02$  for the aspect ratio  $L/H = 3$  and grows to  $-0.026$  for  $L/H = 4$  as in the latter case the cavity is longer and the instabilities have more time and space to develop. A sample of three snapshots over one vortex shedding period  $T$  of the cavity flow is shown in Fig. 6a–c, where the color levels represent the magnitude of the normalized spanwise vorticity  $\omega_z \times H/U_e$  and the isolines highlight vortices in the flow, identified by the  $\lambda_{ci}$  criterion, where  $\lambda_{ci}$  is the swirling strength as introduced by Zhou et al. (1999). The  $\lambda_{ci}$  criterion was here mainly applied to identify large scale structures. Before computing the velocity gradient tensor, using a second-order central difference scheme, a polynomial spatial filter of second-order with a  $5 \times 5$  grid point stencil was applied to the PIV data.

Figure 6 shows a regular spacing of the identified vortices in the shear layer, indicating periodic vortex shedding, which is visually confirmed when observing the time

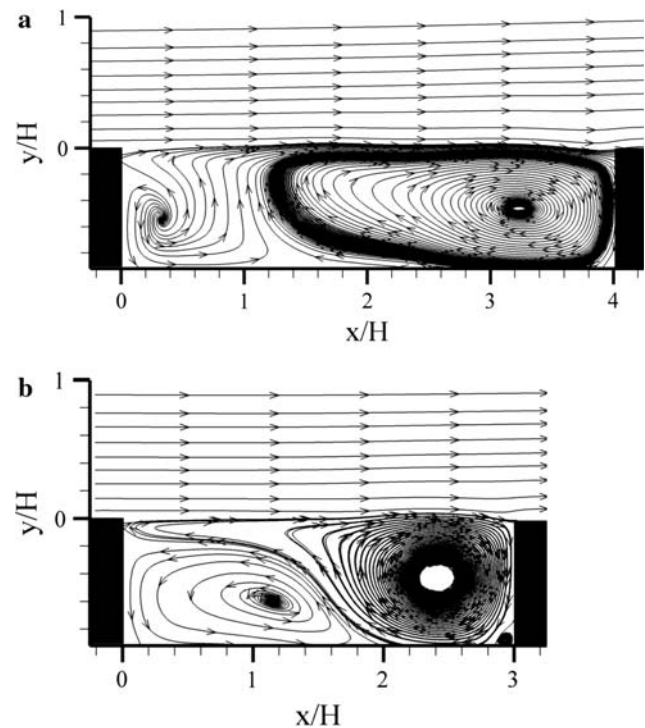


**Fig. 4** Mean streamlines. **a**  $L/H = 4$ . **b**  $L/H = 3$

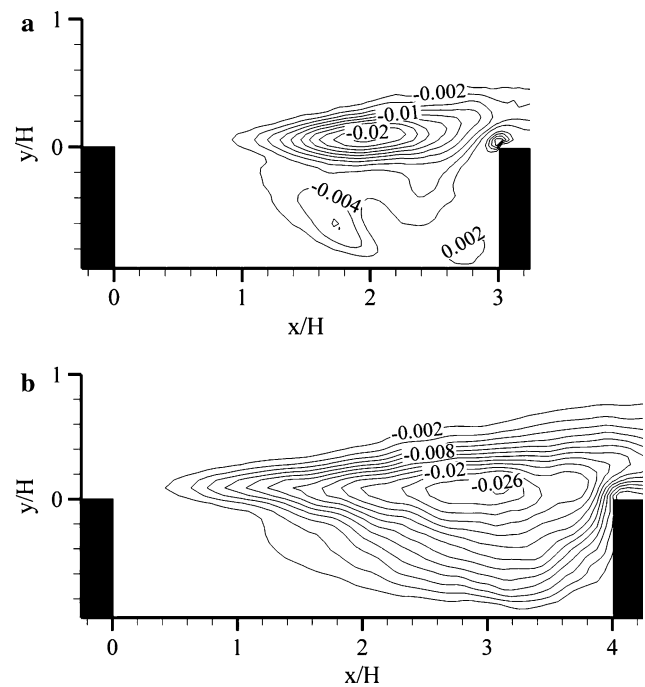


**Fig. 5** Normalized Reynolds shear stress.  $\overline{u'v'}/U_e^2$  **a**  $L/H = 3$ . **b**  $L/H = 4$

animation of the snapshots. The vortices shed inside the shear layer impinge onto the forward facing step and it is nearly always seen, that during the impingement the vortices are divided and one part passes over the cavity trailing

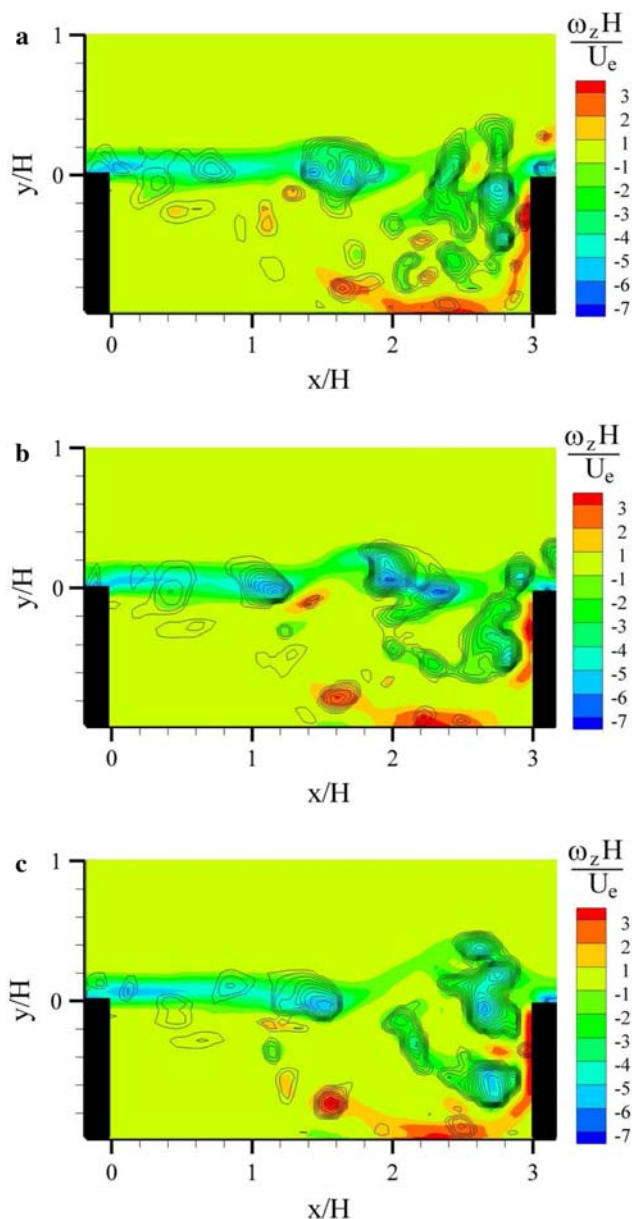


**Fig. 6** Instantaneous vorticity fields  $\omega_z \times H/U_e$  (color plot) and  $\lambda_{ci}$  (isolines) over one vortex shedding period.  $L/H = 3$ . **a**  $t = t_0$ . **b**  $t = t_0 + T/2$ . **c**  $t = t_0 + T$

edge and the other part enters into the cavity. With the larger aspect ratio (see Fig. 7) the vortices are influenced by the downstream recirculation zone, destroying the regular vortex pattern in the downstream area of the cavity. The influence of the downstream recirculation zone in case of  $L/H = 4$  is also seen evaluating the power spectrum of the wall-normal velocity  $v$  at a point in the shear layer close to the cavity trailing edge (Fig. 8). A clear peak is visible at a Strouhal number based on the cavity length  $L$ ,  $St_L = 0.95$ , for both cavities. The observed Strouhal number is very close to the predicted Rossiter mode 2 from

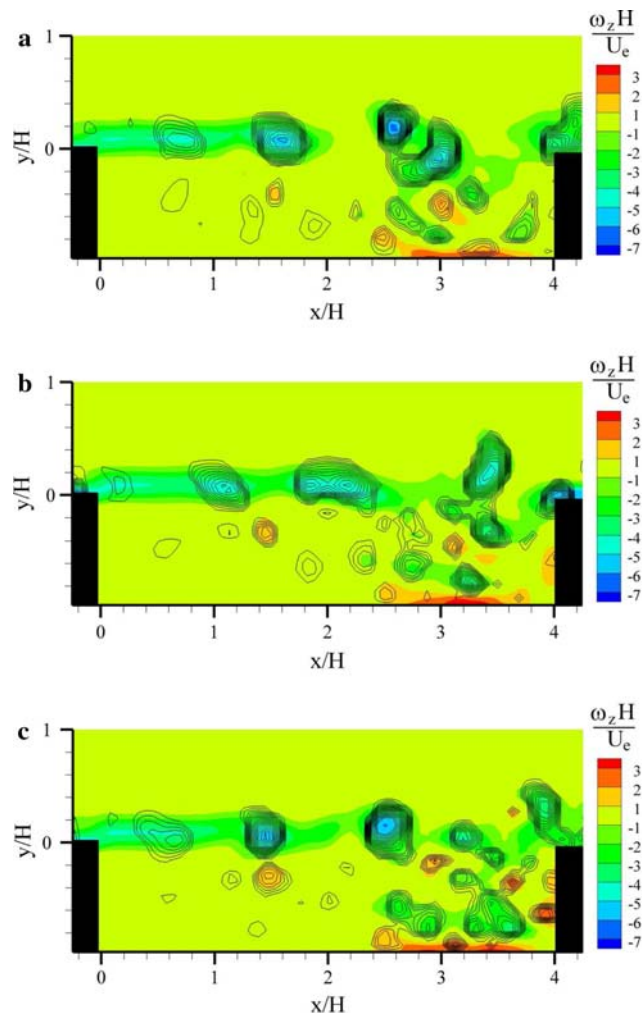


**Fig. 7** Instantaneous vorticity fields  $\omega_z \times H/U_e$  (color plot) and  $\lambda_{ci}$  (isolines) over one vortex shedding period.  $L/H = 4$ . **a**  $t = t_0$ . **b**  $t = t_0 + T/2$ . **c**  $t = t_0 + T$

Eq. 1, which is  $St_{L,R2} = 1$ . However, the peak intensity with the larger aspect ratio is much lower than with the smaller one. This is because with the larger aspect ratio, the downstream recirculation zone impacts on the shear layer instabilities, destroying them and shifting energy from the primary oscillation mode to higher Strouhal numbers. Thus, the velocity spectra becomes broader.

#### 4.2 Instantaneous pressure

Examples of the instantaneous pressure fields are shown in Figs. 9 and 10 over one vortex shedding period. The color levels code the pressure coefficient  $C_p = (p(x, y) - p_\infty) / (0.5\rho U_e^2)$ .

The isolines represent the swirling strength  $\lambda_{ci}$ . Negative minima in the pressure field are found, where the vortex cores are located. The strength of the minima becomes more



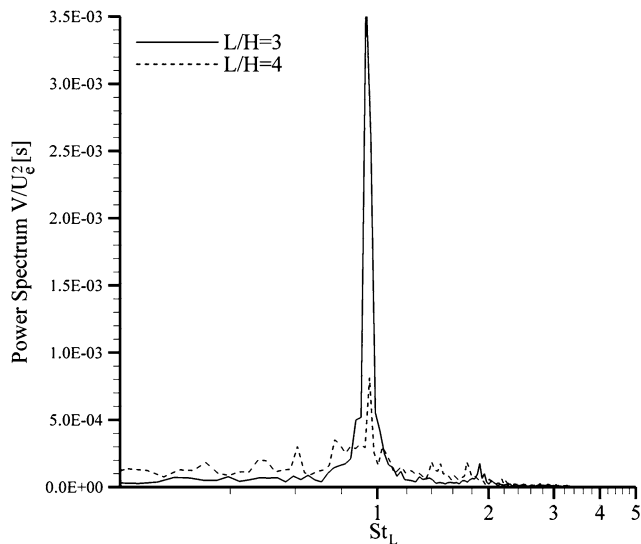


**Fig. 8** Power spectrum of the wall normal velocity at  $x = 0.95L$  and  $y = 0$

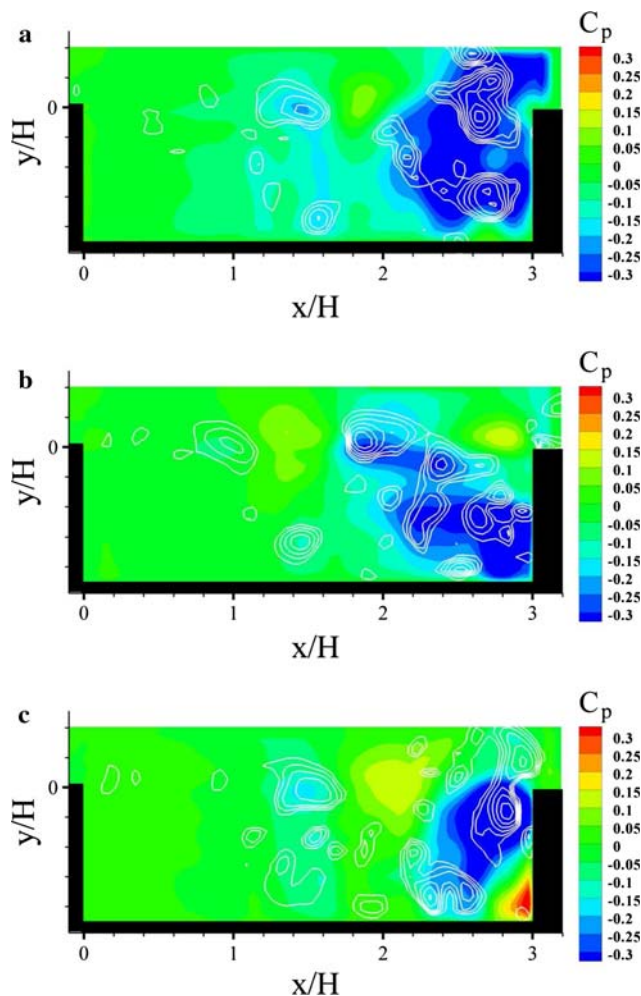


**Fig. 9** Instantaneous pressure coefficient  $C_p$  (color plot) and swirling strength  $\lambda_{ci}$  (isolines).  $L/H = 3$ . **a**  $t = t_0$ . **b**  $t = t_0 + 1/2T$ . **c**  $t = t_0 + T$

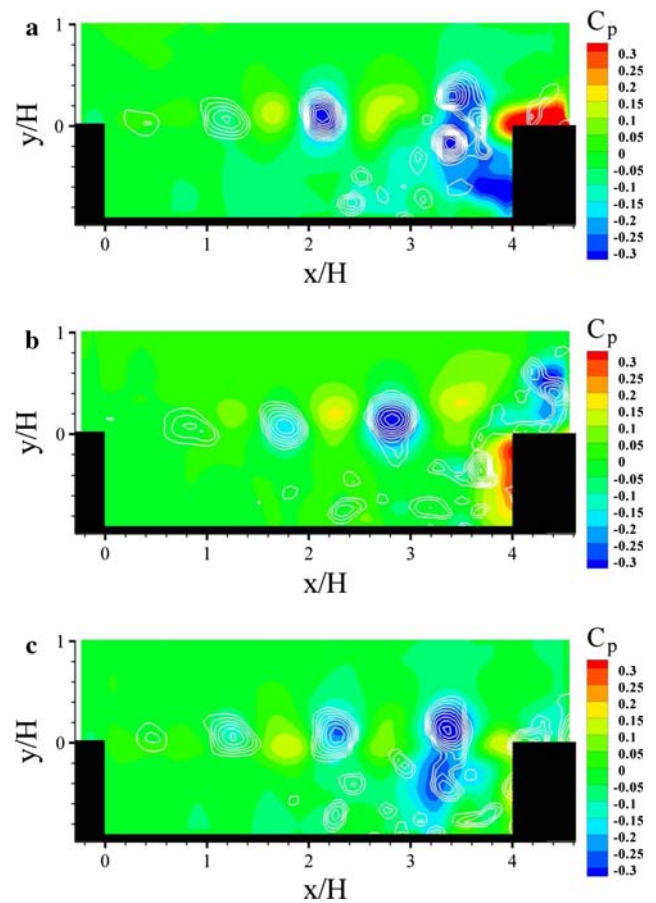


**Fig. 10** Instantaneous pressure coefficient  $C_p$  (color plot) and swirling strength  $\lambda_{ci}$  (isolines).  $L/H = 4$ . **a**  $t = t_0$ . **b**  $t = t_0 + 1/2T$ . **c**  $t = t_0 + T$

negative while the vortices are convected downstream and reach their largest magnitude when reaching the forward facing step. Some of the identified vortices embedded in the recirculation zone do not show a negative pressure core. This is due to the presence of the main recirculation zone that induces stronger accelerations and therefore stronger pressure gradients than the embedded vortices. In between the vortices, regions of high pressure are seen.

In Fig. 11, the spectrum of the pressure coefficient calculated at the same location as in Fig. 8 reveals again a peak at  $St_L = 0.95$ , which confirms that the pressure fluctuations are related to the vortex shedding. Moreover, it is seen that the cavity with the larger aspect ratio exhibits a broader hydrodynamic pressure spectrum, reflecting again the influence of the downstream recirculation zone onto the shear layer instabilities in accordance with the observations in relation to the velocity spectra (see Sect. 5.1). As this mechanism is captured by the analysis of the pressure fluctuations, one can assume a correctly computed temporal and spatial evolution of the pressure field.

The influence of the vortices upon the pressure field can be examined from the two-point correlation function of the

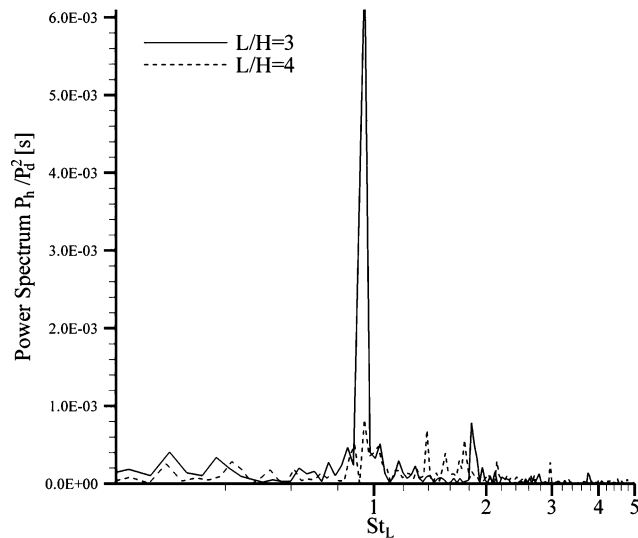


**Fig. 11** Power spectrum of the pressure at  $x = 0.95L$  and  $y = 0$

pressure  $R_{p'p'}$ . Here the correlation is only shown for the aspect ratio  $L/H = 3$  in Fig. 12a, b for two reference points. For a reference position in the shear layer slightly upstream of the cavity trailing edge, the pressure is seen to be correlated only within the shear layer due to the presence of the vortices. A strong correlation to the rest of the field is not seen. The distance from the reference points to the next minimum of the correlation function either upstream or downstream gives half the spacing between two successive vortices. The associated length scale lies around  $1.5H$ .

Figure 12b shows high correlation coefficients above the cavity trailing edge, which indicate that hydrodynamic pressure fluctuations in this area are induced by the passage of the flow over the cavity trailing edge. Observing qualitatively the pressure field time animations, it is noticed that especially the impingement of a vortex onto the forward facing step causes an decrease in pressure above the trailing edge. Finally, Fig. 13 shows the pressure fluctuations normalized by the dynamic pressures  $p_d$ .

#### 4.3 Acoustics

In this section, the time history of 2D pressure fields is used as input to the Curle acoustic analogy of Sect. 3 in order to retrieve information about the sound radiation from the cavities. The pressure time derivative is calculated with a second-order central difference scheme. The surface integral in Eq. 11 is truncated due to the limited field of view, meaning that sound sources which are lying outside the field of view are not considered. Figure 14 shows the spectrum of the acoustic pressure computed at an observer position ( $x = -5H$ ,  $y = 5H$ ).

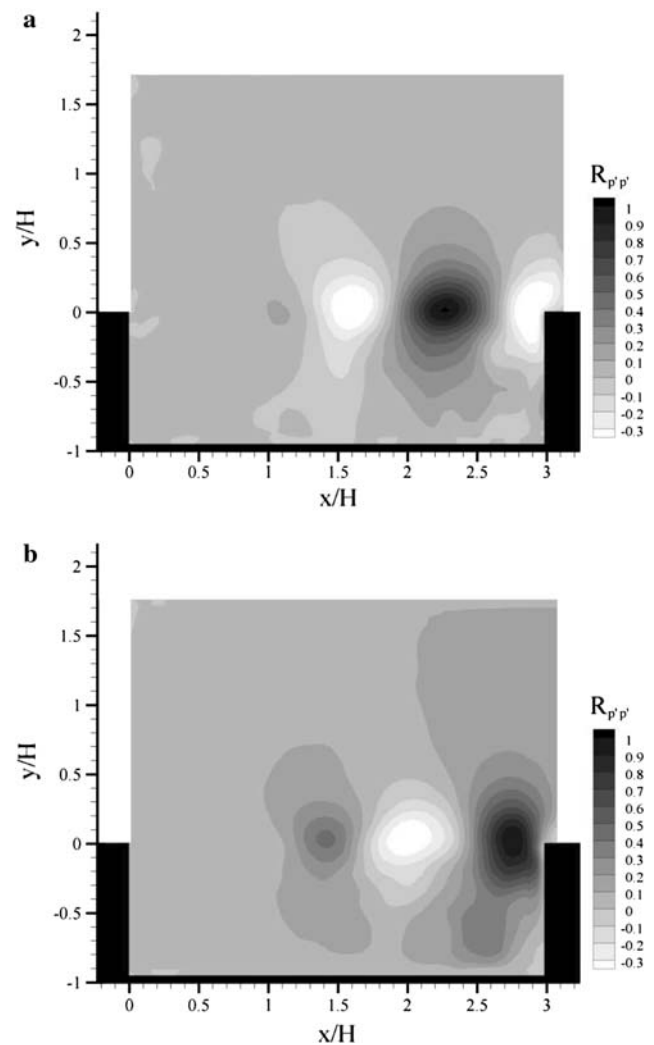


**Fig. 12** Two-point correlation  $R_{p'p'}$  **a**  $x_{ref}/H = 2.3$ ,  $y_{ref}/H = 0$ . **b**  $x_{ref}/H = 2.8$ ,  $y_{ref}/H = 0$

The predicted power spectrum displays a tone at  $St_L = 0.95$ , corresponding to the vortex shedding frequency of the second Rossiter mode. In case of  $L/H = 3$ , the second and the fourth harmonics are visible at  $St_L = 1.9$  and  $St_L = 3.8$ , respectively. Other lower amplitude tones are also shown in Fig. 14, which may be caused by secondary pressure oscillations on the walls, that seem not to be correlated with the vortex shedding. The spectra of the acoustic pressure in case of  $L/H = 4$  show again a broader character with respect to the smaller aspect ratio, which is in accordance with the observation of the velocity and the hydrodynamic pressure fluctuations, see above.

Colonus et al. (2001) found that the far-field acoustic pressure spectrum for a shear layer driven cavity instability is characterized by a single dominant tone, corresponding to the Rossiter mode 2, whereas the corresponding near-field velocity spectra show several tones. Ahuja and Mendoza (1995) find in their experiments that modes 2 and

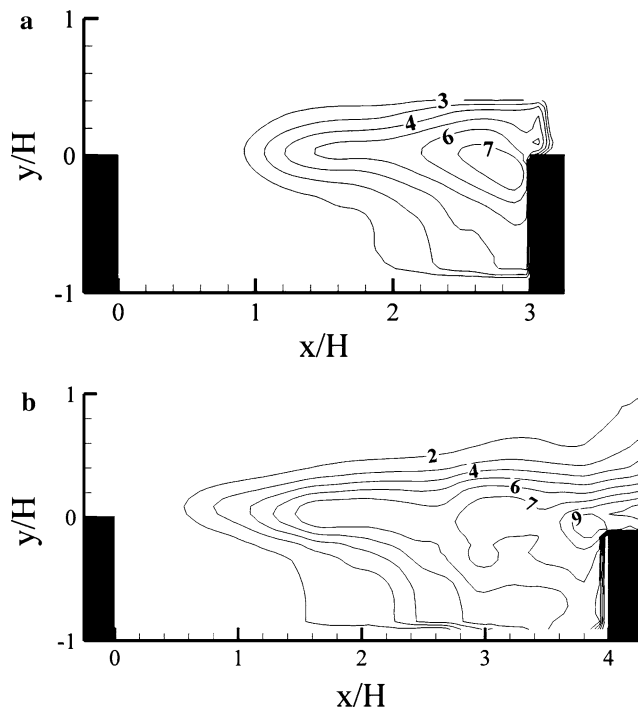


**Fig. 13** Normalized pressure fluctuations  $\overline{p'p'}/p_d^2$  **a**  $L/H = 3$ . **b**  $L/H = 4$

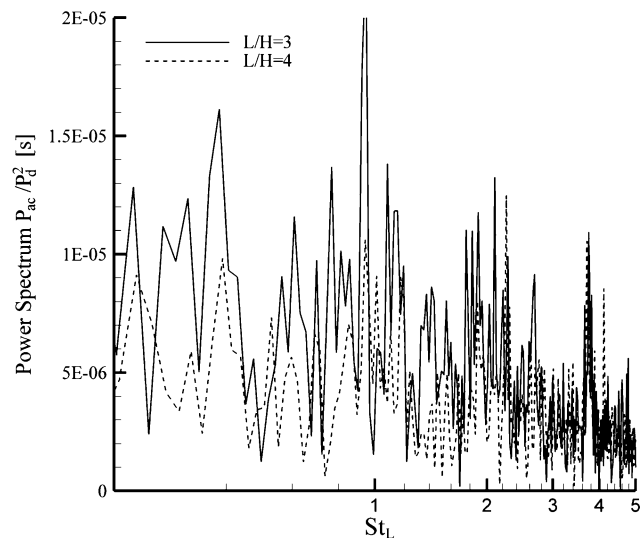


**Fig. 14** Power spectrum of the acoustic pressure at  $x = 0$  and  $y = 7H$

3 are most likely to be dominant in the noise spectra. Further, they note that for larger aspect ratios the acoustic pressure spectra becomes broader, which is consistent with the present study. The origin of this phenomena can be explained with the present results. It is the growing influence of the downstream recirculation zone onto the cavity shear layer instabilities especially in the downstream part of the cavity. The broadening of the spectra of the induced hydrodynamic pressure fluctuations (Sects. 5.1, 5.2) by this

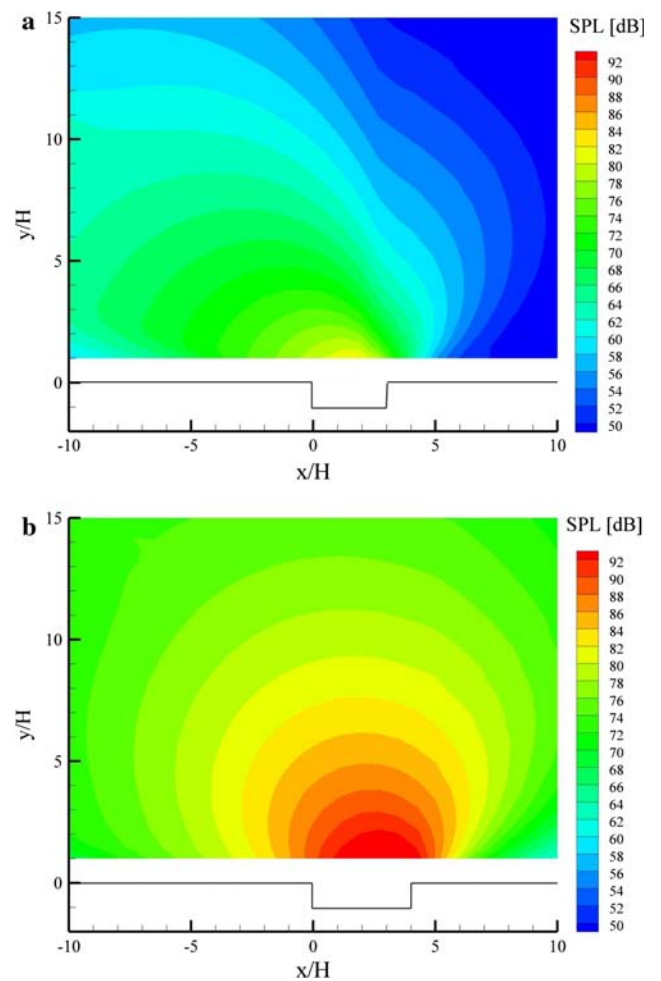


**Fig. 15** Sound pressure level. **a**  $L/H = 3$ . **b**  $L/H = 4$

effect leads to a modification of the sound sources and finally also to a broader acoustic pressure spectrum.

Figure 15 shows the  $SPL = 20\log(p_{rms}/p_{ref})$  above the enclosure, where  $p_{ref} = 0.0002$  Pa. The SPL contours appear to be concentric about the cavity trailing edge, especially in case of  $L/H = 3$ . This confirms that the trailing edge is the main sound source at the selected test conditions.

Further, it is seen that the sound directivity is upstream for  $L/H = 3$ . In Fig. 15a, the azimuthal angle of the upstream noise emission,  $\approx 150^\circ$ , is higher than in the cases studied by Colonius et al. (2001). Ahuja and Mendoza (1995) found that the Rossiter mode 2 has a more uniform directivity than Rossiter mode 3, which contradicts the results of Colonius et al. (2001) and partly the present ones, as in both cases the acoustic spectra show a peak at Rossiter mode 2. However, in case of  $L/H = 4$  a uniform sound emission directivity is found in accordance with Ahuja and Mendoza (1995). Ahuja and Mendoza also found that the preferential sound directivity is downstream for a cavity aspect ratio  $L/H = 1.5$ , and it is upstream and

downstream for larger aspect ratio cavities. A downstream directivity peak is not found here and by Colonius et al. (2001), but by Larsson et al. (2004). Colonius et al. (2001) show a peak directivity angle in the upstream arc of about  $135^\circ$  with respect to the positive  $x$ -axis, whereas this is  $150^\circ$  in the present study. This may be explained considering the very low Mach number of the present flow compared to the higher Mach numbers tested by Colonius et al. (2001). Finally, Ahuja and Mendoza found that larger cavity aspect ratio lead to a more uniform sound emission directivity, which is also found in the present case. The cavity with the larger aspect ratio  $L/H = 4$  shows a uniform sound emission directivity. Discrepancies concerning the directivity of the noise emission in the different cases including the present one, maybe due to the different cavities studied or eventually due to the methodology applied (experimental measurement, direct sound computation, application of hybrid method), which is certainly a question to be studied in the future.

The estimates of far-field cavity noise reported in this section have been derived using a form of the Curle acoustic analogy (Eq. 11), that assumes a finite cavity span and a homogeneous sound source distribution in the spanwise direction. Three-dimensional effects are not taken into account in this way, but should be considered in the future, as they may alternate the sound sources.

## 5 Conclusion

From a time history of 2D velocity fields obtained by PIV the instantaneous 2D pressure fields are obtained, calculating the in-plane pressure gradients via the Lagrangian acceleration and integrating the gradients in space.

Then, a 2D form of the Curle acoustic analogy is applied to the obtained pressure data, where only the line integral over the instantaneous pressure and its time derivative is considered and the quadrupole noise sources in the aerodynamic field are neglected due to their minor contribution.

The methodology is applied to rectangular cavity flows at very low Mach number, with a laminar incoming boundary layer. A regular vortex shedding from the cavity leading edge is observed. The corresponding Strouhal number based on the cavity length is  $St_L = 0.95$ , which is very close to the predicted Rossiter mode 2 ( $St_{L,R} = 1$ ).

The instantaneous pressure fields show minima where the cores of the vortices in the shear layer are located. The impingement of the vortices onto the forward facing step leads to an increase of the strength of the pressure minima and causes lower pressures above the cavity trailing edge.

A main sound source is identified at the cavity trailing edges. The spectrum of the acoustic pressure obtained via the Curle's analogy shows peaks corresponding to Rossiter

mode 2, as well as harmonics of it. Moreover, fluctuating energy is also found at other frequencies, possibly due to pressure fluctuations along the wall, which are not related to the vortex shedding. It is seen that the acoustic pressure spectra is broader in case of the cavity with the larger aspect ratio, which is contributed to the influence of the downstream recirculation zone onto the shear layer instabilities, destroying their regular pattern and ultimately impacting onto the main sound source.

The noise emission from the cavity with the lower aspect ratio is mainly upstream, whereas with the larger aspect ratio the directivity is more uniform, which is consistent with results from Ahuja and Mendoza (1995). It is seen that discrepancies appear concerning the noise emission directivities between different studies, which may be attributed to the specific cavities studied or the methods of sound prediction/measurement applied.

The method described here still needs careful evaluation of errors and verification with experimental and numerical results. When using the pressure along the cavity walls, as required by the Curle's acoustic analogy, it would also be of strong interest to improve PIV algorithms such that velocity data close to the wall becomes more reliable and eventually better resolved.

The present study offers a new experimental methodology to obtain information of the acoustic radiation of a bounded flow while having also information about the sound source respectively the flow feature causing noise radiation. The method offers the possibility to study the sound sources experimentally and trying to alter them in order to reduce noise radiation.

**Acknowledgments** The authors acknowledge Prof. Michele Onorato, Dr. Michele Lovieno and Dr. Aldo Rona for useful discussions and support. This research project has been supported by a Marie Curie Early Stage Research Training Fellowship of the European Community's Sixth Framework Program under contract number MEST CT 2005 020301.

## References

- Ahuja KK, Mendoza J (1995) Effects of cavity dimensions, boundary layer, and temperature on cavity noise with emphasis on benchmark data to validate computational aeracoustic codes. NASA report CR-4653
- Chatellier L, Laumonier J, Gervais Y (2004) Theoretical and experimental investigations of low Mach number turbulent cavity flows. *Exp Fluids* 36:728–740
- Colonius T, Basu AJ, Rowley W (2001) Numerical investigation of the flow past a cavity. *J Fluid Mech* 455:315–346
- Colonius T, Lele SK (2004) Computational aeroacoustics: progress on nonlinear problems of sound generation. *Prog Aerosp Sci* 40:345–416
- Curle N (1955) The influence of solid bodies upon aerodynamic sound. *Proc Royal Soc Lond* 231(1187):505–514
- Elsinga GE, Van Oudheusden BW, Scarano F (2006a) Experimental assessment of tomographic-PIV accuracy. In: 13th international

- symposium on applications of laser techniques to fluid mechanics. Lisbon, Portugal, paper 205
- Elsinga GE, Scarano F, Wieneke B, van Oudheusden BW (2006b) Tomographic particle image velocimetry. *Exp Fluids* 41:933–947
- Ffowcs Williams JE, Hawkins DL (1969) Sound generation by turbulence and surfaces in arbitrary motion. *Philos Trans Roy Soc* 264(1151):321–342
- Gharib M, Roshko A (1987) The effect of flow oscillations on cavity drag. *J Fluid Mech* 177:501–530
- Gloerfelt X, Bogey C, Juve D (2000) Calcul direct du rayonnement acoustique d'unécoulement affleurant une cavité. *Comptes rendus de l'Académie des Sciences (Série IIB)* 328:625–631
- Gloerfelt X, Bogey C, Bailly C, Juve D (2002) Aerodynamic noise induced by laminar and turbulent boundary layers over rectangular cavities. *AIAA paper* 2002-2476
- Gloerfelt X, Bailly C, Juve D (2003) Direct computation of the noise radiated by a subsonic cavity flow and applications of integral methods. *J Sound Vib* 266:119–146
- Grace SM, Dewar WG, Wroblewski DE (2004) Experimental investigation of the flow characteristics within a shallow wall cavity for both laminar and turbulent upstream boundary layers. *Exp Fluids* 36:791–804
- Haigermoser C, Scarano F, Onorato M (2008) Investigation of the flow in a rectangular cavity using tomographic and time-resolved PIV. In: 26th international congress of the aeronautical sciences, Anchorage
- Herrmann J (1980) Least-squares wave front error of minimum norm. *J Opt Soc Am* 70:28–35
- Jensen A, Pedersen GK (2004) Optimization of acceleration measurements using PIV. *Meas Sci Technol* 15:2275–2283
- Komerath NM, Ahuja KK, Chambers FW (1987) Prediction and measurement of flows over cavities. In: *AIAA 25th aerospace sciences meeting*
- Larsson J, Davidson L, Olsson M, Eriksson L (2004) Aeroacoustic investigation of an open cavity at low Mach number. *AIAA J* 42:2462–2473
- Lighthill MJ (1952) On sound generated aerodynamically. *Proc Royal Soc Lond* 211:564–587
- Liu X, Katz J (2006) Instantaneous pressure and material acceleration measurements using a four-exposure PIV system. *Exp Fluids* 41:227–240
- Lyrantzis AS (1994) Review: the use of Kirchhoff's method in computational aeroacoustics. *J Fluids Eng* 116:665–676
- Neise W (2004) Engines as pacemakers for reduction of noise and emission. *ILA*
- Powell A (1953) On edge tones and associated phenomena. *Acustica* 3:233–243
- Powell A (1961) On the edge tone. *J Acoust Soc Am* 33:395–409
- Press WH, Teukolsky SA, Vetterling WT, Flannery BP (2002) *Numerical recipes in C/C++*. The Press Syndicate of the University of Cambridge
- Rockwell D, Naudasher E (1978) Review: self-sustaining oscillations of flow past cavities. *J Fluid Eng* 100:152–165
- Rossiter JE (1964) Wind-tunnel experiments on the flow over rectangular cavities at subsonic and transonic speeds. *Aeronautical Research Council*
- Rowley W, Colonius T, Basu AJ (2001) On self-sustained oscillations in two-dimensional compressible flow over rectangular cavities. *J Fluid Mech* 455:315–346
- Rowley CW, Williams DR (2006) Dynamics and control of high-Reynolds-number flow over open cavities. *Annu Rev Fluid Mech* 38:251–276
- Sarkar S, Hussaini MY (1993) *Computation of the acoustic radiation from bounded homogeneous flows*. Computational Aeroacoustics. Springer, New York, pp 335–354
- Rona A (2007) The acoustic resonance of rectangular and cylindrical cavities. *J Algorithms Comput Technol* 1:329–355
- Sarohia V (1977) Experimental investigation of oscillations in flows over shallow cavities. *AIAA J* 15:984–991
- Shieh CM, Morris PJ (1999) Parallel numerical simulation of subsonic cavity noise. *AIAA Paper* 99-1891
- Southwell WH (1980) Wave-front estimation from wave-front slope measurements. *J Opt Soc Am* 70:998–1006
- Stratton JA (1941) *Electromagnetic theory*. International Series in Pure and Applied Physics
- Takeda K, Shieh CM (2004) Cavity tones by computational aeroacoustics. *Int J Comput Fluid Dyn* 18:439–454
- Tam C, Block P (1978) On the tones and pressure oscillations induced by flow over rectangular cavities. *J Fluid Mech* 89:373–399
- Tam CKW (2004) Computational aeroacoustics: an overview of computational challenges and applications. *Int J Comput Fluid Dyn* 18:547–567
- Zhou J, Adrian RJ, Balachandar S, Kendall TM (1999) Mechanisms for generating coherent packets of hairpin vortices in channel flow. *J Fluid Mech* 387:353–396